A Novel Analog Control Strategy With Simplified Implementation Scheme for Boundary Conduction Mode Flyback Microinverter

Celiang Deng, Min Chen, *Member, IEEE*, Fan Zhang, Ruirui Zheng, and Feng Jiang

***Abstract*—With the continuous reduction in the per-watt cost of photovoltaic modules, the complexity and cost of the controller circuit are becoming one of the key factors limiting the competitiveness of flyback microinverters in cost-sensitive PV applications. To address this issue, this article proposes a novel analog control strategy for boundary conduction mode flyback microinverters. This strategy utilizes a minimal number of basic analog components to achieve low total harmonic distortion in grid-connected current and high static and dynamic MPPT efficiencies. To enable peak-current control, a dedicated analog divider circuit, consisting of only three basic components, is designed to perform complex computations typically required for the traditional current reference. Using this divider, low harmonic distortion grid-connected current and a high power factor can be achieved. In addition, an improved analog MPPT strategy with optimized perturbation logic and control timing is introduced to simplify the hardware implementation and eliminate misjudgment issues caused by the double-line frequency power fluctuations. The improved strategy enables both high efficiency and stable MPPT control without the need for additional timers and signal conditioning circuits. Experimental results on a 125 W prototype are presented to validate the advantages of the proposed analog control strategy.**

***Index Terms*—Analog control, flyback, maximum power point tracking (MPPT), microinverter, photovoltaic (PV).**

I. Introduction

MICROINVERTER is favored for its safety, independence, and convenience [1]. The global solar microinverter market is expected to grow at a CAGR of 18.9% from 2024 to 2030 [2]. The compact size, high efficiency, and simplified design of microinverters have become the trend.

Microinverters, from the very beginning, have consistently faced the problem of high per-watt cost compared to central inverters and string inverters [3], and as advancements in high-efficiency photovoltaic technologies continue, the cost issue has become increasingly significant. The per-watt cost of PV modules has significantly decreased from 0.68$/W in 2015 to 0.12$/W in 2024 [4]. The efficiency of commercial PV modules has reached 24%–25% under standard test conditions [5] and continues to improve. In addition, next-generation PV technologies (organic materials, quantum dots, and hybrid organic–inorganic materials) are also rapidly developing, such as perovskite/crystalline silicon tandem solar cells under laboratory conditions has reached 34.6% [5]. Both of these trends indicate a further decrease in the per-watt cost of PV modules.

Therefore, although the per-watt cost of microinverters has dropped from 0.60$/W in 2011 to 0.20$/W in 2024, further cost reductions are crucial for improving the overall economic benefits of PV systems, particularly in cost-sensitive, low-power applications. Low-power PV systems, typically rated below 800 W, can be installed without an electrician and registered easily in Europe [6]. They serve as attractive sources of self-consumption electricity for tenants and apartment dwellers. These systems, with their short payback cycle, are expected to be as popular as home appliances. The installation of low-power plug-in PV systems in Germany reached 1 million units by the end of 2023 [7], underscoring a growing trend in this market.

Initially, flyback converters were widely adopted in low-power LED driver applications as a single-stage power factor corrector (PFC) because of their simple structure, high boost ratio, electrical isolation, and low cost. These advantages later made them become one of the most successful commercial microinverter topologies [8], [9]. Analog control schemes [10], [11], [12] have been widely used in low-power single-stage flyback (SSF) PFCs for their low cost. SSF PFCs and SSF microinverters are symmetrical in circuit structure, making analog control strategies attractive for cost-sensitive PV systems.

Flyback converters usually work in discontinuous conduction mode (DCM) and continuous conduction mode (CCM) for control simplification [11], and automatical high power factor (PF) [12]. CCM can offer higher power density, but the transfer function of control-to-output-current introduces a right-half-plane zero, complicating controller bandwidth design [42], [43]. A unit PF can be obtained by modulating the main switch's ON-time [13], [14], [17], [19] or peak-current [15], [16], [18], [20], [21]. In particular, the control scheme in [18] has been applied in commercial products for nearly a decade. These methods focus on improving weighted efficiency and reducing the total harmonic distortion (THD), resulting in complex algorithms. Therefore, they are typically implemented using digital controllers such as DSP or FPGA for convenience. However, some real-time control

Received 5 November 2024; revised 25 December 2024; accepted 24 January 2025. Date of publication 13 February 2025; date of current version 20 March 2025. This work was supported by the National Natural Science Foundation of China under Grant 51877195. Recommended for publication by Associate Editor M. Ordonez. *(Corresponding author: Min Chen.)*

The authors are with the College of Electrical Engineering, Zhejiang University, Hangzhou 310027, China (e-mail: 12210061@zju.edu.cn; calim@zju.edu.cn; 22210036@zju.edu.cn; 22010076@zju.edu.cn; jiangfeng@zju.edu.cn).

Color versions of one or more figures in this article are available at https://doi.org/10.1109/TPEL.2025.3538078.

Digital Object Identifier 10.1109/TPEL.2025.3538078

methods, such as peak-current control (PCC), still require digital controllers combined with digital-to-analog converter (DAC) and analog comparators [15], [18] to improve precision during high-speed operations. These digital or mixed digital–analog schemes have complex structures, making straightforward analog designs challenging.

Fortunately, with the emergence of appropriate MPPT strategies [22], [23], analog control strategies for DCM flyback microinverters [3], [24], and analog interleaving control method [25], it is possible to make progress in the analog control scheme for BCM flyback microinverters. However, some new challenges may arise with direct adoptations of mature grid-connected control methods from flyback PFCs and analog MPPT methods from dc/dc PV applications.

First, grid-connected control for microinverters is more complicated due to the difference in input/output voltage. The DCM flyback PFC has an innate sinusoidal input current [11] under constant on-time control, owing to its folded sinusoidal input voltage. However, DCM flyback microinverters require modulating the duty cycle to a sinusoidal shape, which needs an extra multiplier [24], achievable using PWM ICs like L6561 or TDA4863. The BCM flyback PFC uses two analog multipliers to reduce current distortion [10], which is similar to BCM flyback microinverters where the current reference contains a sine square term [15]. A variable on-time control method [26], [36] was proposed for BCM flyback PFCs to eliminate one multiplier by using input and output voltages to modulate the main switch's ON-time. However, this method cannot be directly applied to microinverters due to their nonsinusoidal input voltage, requiring additional circuitry. One-cycle control [11], [27] is another low-cost peak-current modulation strategy for low-power PFCs, but it is designed to meet the PFC harmonics standard (IEC 61000-3-2) of 10%, and it exhibits a THD exceeding 5%, which does not comply with the harmonic standards for microinverters (IEC 61727 and IEEE 1547). Although analog control strategies employed in flyback PFCs offer valuable insights for microinverters, directly adapting these methods tends to increase circuit complexities and costs.

The second challenge pertains to implementing a simple, high-performance analog MPPT strategy tailored for microinverters. Several commercial enterprises have introduced dedicated MPPT chips designed for PV dc/dc applications, like SPV1020, LT8490, and SM72441. These chips integrate the perturbation and observation (P&O) MPPT module, a digital signal processing core, and analog-to-digital converters (ADCs). Notably, ADCs typically occupy a substantial die area, with two 8-bit ADCs fabricated using a 0.35 μm CMOS process consuming approximately double the area of the analog MPPT module [28]. Consequently, analog MPPT is very attractive for cost-sensitive PV applications.

Many analog implementation methods of the P&O and incremental conductance (INC) algorithms have been proposed for dc/dc PV applications due to their simple principles. The P&O MPPT can be achieved by only perturbating and observing a single variable [22], [23], [29], [30], offering a simple circuit design suitable for most PV applications. An analog INC method, proposed in [31], used two peak detector circuits and a passive high-pass filter, resulting in a complex circuit and poor high-frequency noise suppression capabilities. To simplify the detection, Mattavelli et al. [32] used the MOSFET's linear region to measure and store conductance values of the PV module, but still requires a microcontroller (FPGA, DSP) to control the duty cycle. Therefore, the analog P&O method in [23] is most suitable for flyback microinverters in terms of circuit structure and cost. However, directly applying the analog P&O scheme in microinverters may result in MPPT misjudgment due to the double-line frequency fluctuations in the PV output power [21]. Typically, using the average value of the output power in half a line cycle to execute the MPPT can effectively eliminate the misjudgment [3], but this results in a complicated circuit. This article focuses on using basic analog components to detect the variation trend of output power and eliminate the influence of double-line frequency fluctuations on the MPPT perturbation control logic.

Motivated by the potential of analog control schemes in BCM flyback microinverters, this article aims to utilize a minimal number of basic analog components to achieve low THD in grid-connected current and high static and dynamic MPPT efficiencies. To enable PCC, a dedicated analog divider, consisting of only three basic components, is incorporated into the current reference generation circuit to perform complex computations. In addition, an analog MPPT strategy with optimal perturbation logic and control timing is introduced to simplify the hardware implementation and eliminate misjudgment issues.

The rest of this article is organized as follows. Section II analyzes the realization of the proposed analog control strategy, including the PV system configuration, the operation principle of the analog divider and its bandwidth design principle, the analog MPPT control strategy, and the corresponding parameters design. Section III presents considerations for efficiency improvements and the THD reduction of the grid-connected current. The experimental results based on a 125 W prototype are demonstrated in Section IV. Section V compares the existing BCM control schemes with the proposed method and provides application prospects. Finally, Section VI concludes this article.

II. Proposed Analog Control Principle

A. PV System Configuration

For higher power density and overall efficiency improvements, BCM is selected as the operating mode for the flyback microinverter. To directly control the primary current i_p, the PCC method is used to obtain a sinusoidal grid-connected current by modulating the peak value of i_p according to the current reference $i_{p\_\text{peak}}(\theta_g)$.

The circuit structure of the proposed BCM flyback microinverter is shown in Fig. 1(a). In the main power circuit, the inverter with a pseudo-dc link turns a rectified current waveform into a sinusoidal waveform by utilizing an unfolding bridge, which avoids losses caused by high-frequency switches [15]. In the control circuit, the power reference, P_{ref}, is generated by the analog MPPT control circuit and transferred to the analog divider. The output signal of the divider, v_{div}, is used to generate $i_{p\_\text{peak}}(\theta_g)$. Thus, the MPPT can be achieved by applying a perturbation to P_{ref}.

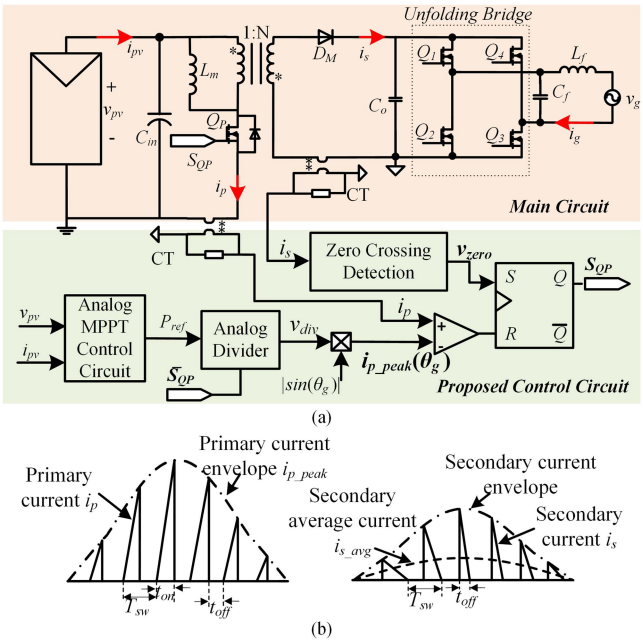

Fig. 1. (a) Proposed BCM flyback microinverter configuration. (b) Current waveforms of BCM flyback microinverter in half a line cycle.

The key waveforms of the inverter in half a line cycle are depicted in Fig. 1(b). The primary current i_p and the zero-crossing signal v_{zero} of the secondary current, i_s, are detected by the noninvasive current transformer (CT). When i_p reaches the current reference, i.e., the primary current envelope, the reset–set (RS) trigger flips the output signal S_{QP} to "0," and the main switch Q_P turns OFF. On the contrary, as the secondary current arrives at the zero-crossing point, Q_P turns ON.

Since the switching frequency is much higher than the line frequency in the actual working process, to simplify the analysis, it can be considered that the PV voltage and the grid voltage remain unchanged within a switching period. The average value of the secondary current in a switching period can be expressed as

$$i_{s\_\text{avg}}(\theta_g) = \frac{1}{2}\frac{i_{p\_\text{peak}}(\theta_g)}{N}\frac{t_{\text{off}}}{t_{\text{on}}+t_{\text{off}}} = \frac{1}{2}\frac{i_{p\_\text{peak}}(\theta_g)}{N}d'(\theta_g) \quad (1)$$

where t_{off} is the turn-OFF duration of the main switch Q_P. t_{on} is the turn-ON duration of Q_P. $d'(\theta_g)$ represents the complementary duty cycle of Q_P and equals $t_{\text{off}}/(t_{\text{on}}+t_{\text{off}})$. θ_g ($\theta_g = \omega_g t$) is the phase angle of the utility grid. N is the transformer turns ratio. The PV voltage fluctuations can be ignored as the input capacitance is large enough, and the steady-state value of $d'(\theta_g)$ varies monotonically with $\sin(\theta_g)$ [15]

$$d'(\theta_g) = \frac{t_{\text{off}}}{t_{\text{on}}+t_{\text{off}}} = \frac{N v_{\text{pv}}}{\sqrt{2}V_g \sin(\theta_g) + N v_{\text{pv}}} \quad (2)$$

where V_g is the root-mean-square value of the grid voltage, and v_{pv} is the instantaneous voltage of the PV module. The secondary current is injected into the utility grid through the *CL* filter, and $i_{s\_\text{avg}}(\theta_g)$ equals the instantaneous value of the grid-connected current i_g. To obtain a sinusoidal waveform of $i_{s\_\text{avg}}(\theta_g)$, the current reference can be designed as

$$i_{p\_\text{peak}}(\theta_g) = \frac{2\sqrt{2}N}{V_g}\frac{P_{\text{ref}}}{d'(\theta_g)}\sin(\theta_g). \quad (3)$$

Generating $i_{p\_\text{peak}}(\theta_g)$ is easier with digital control chips than with analog circuits. The main challenge for analog schemes is accurately performing the division operation $P_{\text{ref}}/d'(\theta_g)$ with dedicated function components. One way is to use a multiplier circuit, which is connected to the feedback path of an operational amplifier. Another approach involves subtracting the outputs of two logarithmic networks and then applying an antilogarithmic operation to the resulting difference. Integrated circuits (ICs) like the MPY100 and AD633 can handle these operations, but analog multipliers are often expensive.

To reduce costs, some alternatives used discrete components. For example, Sanchez-Sinenci et al. [33] proposed an analog divider based on the current-source characteristics of a voltage-controlled operational transconductance amplifier, while Laoppoulos and Karybakas [34] proposed a method using a voltage-controlled oscillator to convert voltage into a pulse signal. Additionally, Liu and Chang [35] employ differential amplifiers and transistors in saturation for division. The inputs of these high-precision divider circuits are analog voltage signals. Therefore, a signal conversion circuit is necessary to convert a PWM signal into a voltage signal when used to perform the division calculation of (3). However, this will result in greater circuit complexity and increase the overall system cost.

Regarding the implementation of the MPPT algorithm in analog circuits, although many analog-based MPPT circuits have been proposed for dc/dc PV applications [22], [23], [29], [30], [31], [32], when applied directly to PV microinverters, new challenges such as increased circuit complexity and higher costs may arise.

To address the challenges related to circuit complexity and cost mentioned earlier, a dedicated analog divider is proposed to simplify the current reference generation process, reducing component count and enhancing system performance. Furthermore, an analog MPPT strategy is proposed to optimize the MPPT perturbation logic and eliminate misjudgment issues.

B. Operation Principle of Analog Divider Circuit

Due to the variable frequency characteristics of the BCM flyback microinverter, it is hard to obtain the current reference $i_{p\_\text{peak}}(\theta_g)$ under the analog scheme. By taking advantage of the ampere–second balancing characteristics of the capacitor, an analog divider circuit is proposed, as shown in Fig. 2. $v_{\text{ref}}(t)$ is the input voltage and $v_{\text{out}}(t)$ is the output voltage. g represents the transfer conductance of the voltage-controlled current source. S_1 and S_2 are signal switches controlled by the complementary driving signal, $\bar{S}_{QP}$, of the main switch without the need for extra drive circuits.

Fig. 3 shows the steady-state waveforms of the analog divider. During one switching period, the working condition of the analog divider can be divided into two stages.

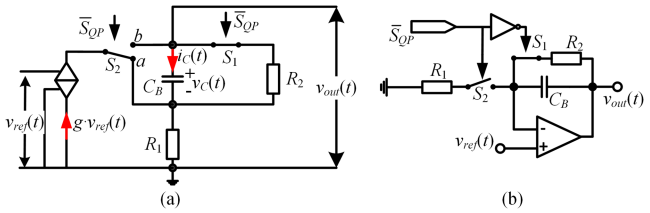

Fig. 2. (a) Simplified block diagram of divider circuit. (b) Hardware implementation.

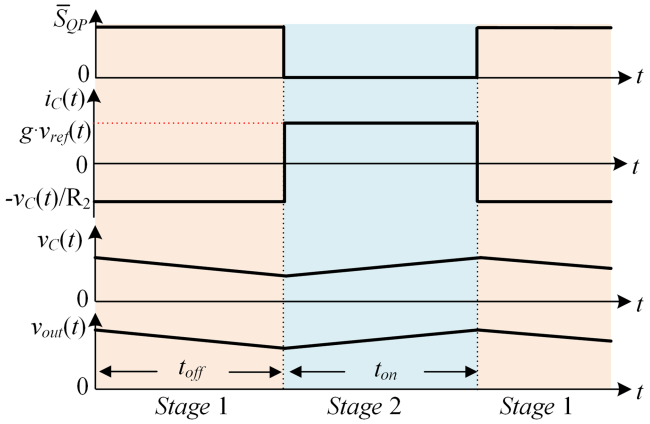

Fig. 3. Key waveforms of the analog divider circuit.

Stage 1: When $\bar{S}_{QP}$ is at 1, S_1 is turned ON, S_2 is linked to "*a*," and the capacitor C_B is discharged. The discharging current equals $-v_C(t)/R_2$. The time duration of Stage 1 equals the turn-OFF time t_{off} of the main switch.

Stage 2: When $\bar{S}_{QP}$ is at 0, S_1 is turned OFF and S_2 is linked to "*b*," and C_B is charged. The charging current equals $g{\cdot}v_{\text{ref}}(t)$. The time duration of Stage 2 equals the turn-ON time t_{on} of the main switch.

According to the ampere–second balance principle of C_B in one switching period, we have

$$\langle v_C(t)\rangle_{T_s} = \frac{d(t)}{d'(t)} \cdot g\langle v_{\text{ref}}(t)\rangle_{T_s} R_2 \tag{4}$$

where $< v_C(t) >_{Ts}$ and $< v_{\text{ref}}(t) >_{Ts}$, respectively, represent the average value of $v_C(t)$ and $v_{\text{ref}}(t)$ in one switching period. The average output voltage of the divider circuit over one switching period, $< v_{\text{out}}(t) > Ts$, is equivalent to the voltage drop across capacitor C_B and resistor R_1

$$\langle v_{\text{out}}(t)\rangle_{T_s} = \left(R_1 g + \frac{d(t)}{d'(t)} R_2 g\right) \langle v_{\text{ref}}(t)\rangle_{T_s}. \tag{5}$$

Set $R_1 = R_2$ and $g = 1/R_1$. Since the switching frequency is much higher than the line frequency, the relationship between $v_{\text{out}}(t)$ and $v_{\text{ref}}(t)$ can be expressed as follows according to (5):

$$v_{\text{out}}(t) = v_{\text{ref}}(t)/d'(t). \tag{6}$$

The division operation function required by $d'(t)$ can be achieved through the proposed analog divider circuit, and the circuit cost can be reduced owing to the simple circuit structure.

C. Design of Analog Divider Circuit

The output signal of the analog divider is used to generate the current reference $i_{p\_\text{peak}}(\theta_g)$, thus directly impacting the quality of the grid-connected current. The resistance R_2 and capacitance C_B in the analog divider constitute a low-pass filter, and an improper bandwidth may result in distorted output waveforms of the divider. Therefore, by constructing the small-signal transfer function from $d'(t)$ to $v_C(t)$ and analyzing the bode diagram, bandwidth constraints are derived to achieve output waveforms with minimized distortion.

The average value of the current flowing through the capacitor C_B in one switching period can be obtained as

$$\begin{aligned}\langle i_C(t)\rangle_{T_s} &= -\frac{\langle v_C(t)\rangle_{T_s}}{R_2} \cdot d'(t) + d(t) \cdot g\langle v_{ref}(t)\rangle_{T_s} \\ &= C_B \frac{d\langle v_C(t)\rangle_{T_s}}{dt}.\end{aligned} \tag{7}$$

The small-signal equation for the capacitor voltage $v_C(t)$ can be obtained from (7)

$$\begin{aligned}C_B \frac{d\hat{v}_C(t)}{dt} + \frac{d'(t)}{R_2}\hat{v}_c(t) &= g\left(1 - d'(t)\right)\hat{v}_{\text{ref}}(t) \\ &\quad - \left(gV_{\text{ref}} + \frac{V_C}{R_2}\right)\hat{d}'(t)\end{aligned} \tag{8}$$

where V_C is the steady-state value of $v_C(t)$ and V_{ref} is the steady-state value of $v_{\text{ref}}(t)$. Based on (8), the small-signal transfer function from $\hat{d}'(t)$ to$\hat{v}_C(t)$ can be expressed as

$$\begin{aligned}G_{\text{div}}(s)\big|_{\hat{v}_{\text{ref}}(s)=0} &= \frac{\hat{v}_C(s)}{\hat{d}'(s)} = \frac{gR_2V_{\text{ref}} + V_c}{C_BR_2s + d'(t)} \\ &= Z_{\text{div}} \cdot \frac{1}{s/\omega_{\text{div}} + 1}\end{aligned} \tag{9}$$

where

$$Z_{\text{div}} = \frac{gR_2V_{\text{ref}} + V_c}{d'(t)}, \qquad \omega_{\text{div}} = \frac{d'(t)}{C_BR_2}. \tag{10}$$

ω_{div} is the corner frequency. The bode diagram of $G_{\text{div}}(s)$ at a steady state ($d' = 0.4$, $V_{\text{ref}} = 0.8$ V, $V_C = 1.2$ V) is shown in Fig. 4. The numerical simulation results are consistent with the theoretical values, and it shows that $G_{\text{div}}(s)$ possess the low-pass characteristic.

In the steady state, according to (2), the value of $d'(t)$ changes by the phase angle. Thus, ω_{div} will also undergo variations according to (10). Based on (2) and (10), the maximum value of ω_{div} can be obtained as

$$\omega_{\text{div\_max}} = \frac{1}{C_BR_2}. \tag{11}$$

Furthermore, the minimum value of ω_{div} can be derived as

$$\omega_{\text{div\_min}} = \frac{1}{C_BR_2} \frac{Nv_{\text{pv}}}{\sqrt{2}V_g + Nv_{\text{pv}}}. \tag{12}$$

To achieve the distortion-free output waveform, the bandwidth should be accurately designed to pass through the line frequency component in $d'(t)$, while effectively filtering out

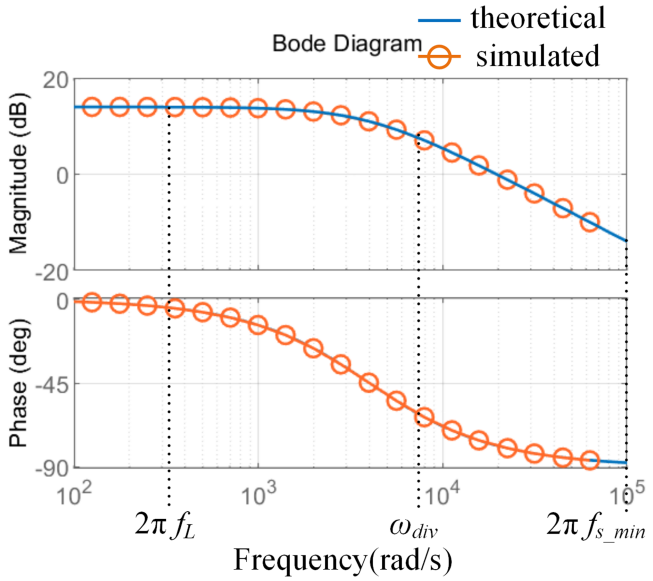

Fig. 4. Bode diagram of $G_{div}(s)$.

the switching frequency component. Based on this criterion, a constraint on ω_{div} can be obtained as

$$\omega_{div\_min} \geq 10 * 2\pi f_L, \quad \omega_{div\_max} \leq 2\pi f_{s\_min}/10 \tag{13}$$

where f_L is the line frequency and f_{s_min} is the minimum switching frequency of the main switch Q_P.

Therefore, the value of R_2 can be obtained according to (11)–(13) once the value of C_B is well-designed. The capacitance C_B can be determined by the voltage ripple tolerance

$$C_B = \frac{gV_{ref}t_{on\_max}}{\Delta V_{C\_tol}} \tag{14}$$

where ΔV_{C_tol} is the voltage ripple tolerance of C_B and is set to 1% of the steady-state value V_C based on experimental experience. t_{on_max} is the maximum turn-ON time of Q_P and is set to $1/(2f_{s\_min})$, which equals half the maximum switching period.

Fig. 5 shows the output simulation waveforms of the analog divider across three different bandwidths based on the PLECS platform. It is evident that only when ω_{div} satisfies the design criteria (13) does the output waveform of the divider exhibit no significant distortion.

D. Analog MPPT Strategy

A dedicated MPPT implementation scheme is proposed to simplify the MPPT perturbation logic and mitigate misjudgment issues without the need for additional signal conditioning circuits and timers. Moreover, a single voltage loop is employed to enhance the system stability, particularly during rapid changes in irradiation.

P_{ref} is designed as the control variable for the MPPT perturbation operation as mentioned in Section II-A. The power versus voltage curve of the PV module and the MPPT perturbation

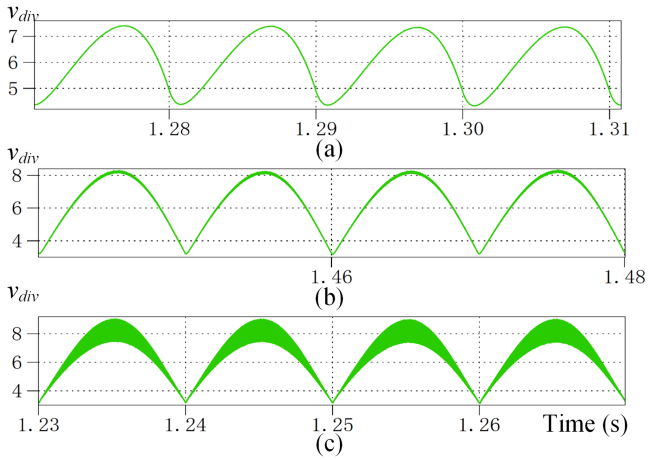

Fig. 5. Output signals of the proposed analog divider with different values of corner frequency: (a) $\omega_{div\_max} = 1000$ rad/s, (b) $\omega_{div\_max} = 10\,000$ rad/s, and (c) $\omega_{div\_max} = 100\,000$ rad/s.

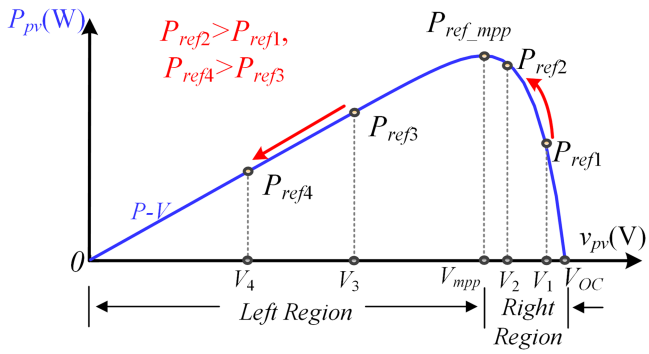

Fig. 6. MPPT perturbation process.

TABLE I
LOGICAL ANALYSIS

V_{flag2}	V_{pw_dir}	V_{flag1}
0	0	1
0	1	0
1	0	0
1	1	1

workflow are shown in Fig. 6, where V_{OC} represents the open-circuit voltage. The working principle of the proposed MPPT is similar to that of the P&O method, where the perturbation direction for the next cycle is determined by both the perturbation and power variation directions in the previous cycle. For instance, an increase in P_{ref} shifts the operating point from P_{ref1} to P_{ref2}, indicating a movement toward the MPP. Consequently, P_{ref} should continue to be adjusted in the same direction to further approach the MPP. The relationship between the change directions of P_{ref} and P_{pv} in the current working cycle denoted as V_{flag2}, V_{pw_dir}, and the perturbation direction of P_{ref} for the next working cycle, denoted as V_{flag1}, can be summarized in Table I.

For convenience, it is necessary to define the increase of P_{ref} and P_{pv} as "1," and the decrease as "0." Through the analysis of Table I, the relationship between V_{flag2}, V_{pw_dir}, and V_{flag1} can

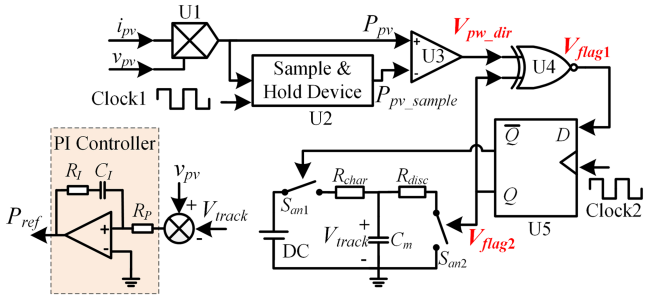

Fig. 7. Circuit structure of the analog MPPT control circuit.

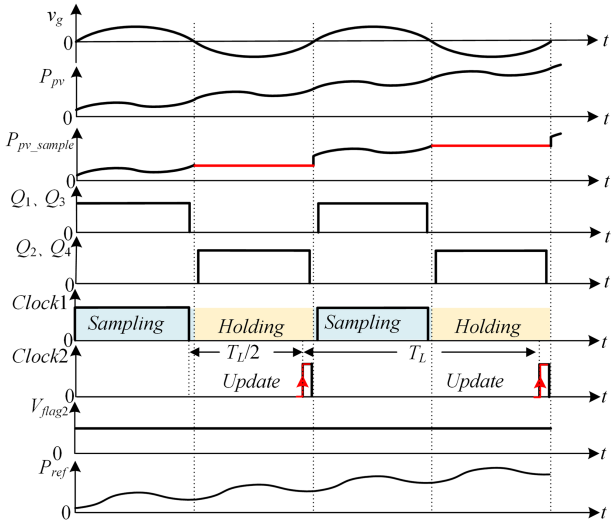

Fig. 8. Theoretical waveforms of the proposed analog MPPT controller.

be obtained as

$$V_{\text{flag}\,1} = V_{\text{flag}\,2} V_{\text{pw\_dir}} + \bar{V}_{\text{flag}2} \bar{V}_{\text{pw\_dir}}. \tag{15}$$

Table I covers all working situations, therefore, based on the perturbation logic (15), the MPPT controller can force the operating point to move toward the MPP under any irradiation conditions. Thus, there exists a specific value, $P_{\text{ref\_mpp}}$, that makes the system operate at the MPP.

Based on Table I, an analog MPPT control circuit is proposed, as shown in Fig. 7. The hardware implementation is remarkably simple using only one multiplier U1, one sample and hold device (S&H) U2, one comparator U3, one XNOR logic device U4, and one D-type flip-flop U5. U1–U5 are used to realize the logical operation of Table I, and two analog switches S_{an1} and S_{an2} are used to convert the logical signal V_{flag2} into the analog signal V_{track}. A type IIa compensator (PI controller), of which the parameters design will be presented in Section II-E, is utilized to track the voltage reference, V_{track}.

The theoretical waveforms of the analog MPPT circuit are shown in Fig. 8. The driving signals of Q_1–Q_4 are obtained through the zero-crossing detection of the grid voltage. Clock1 is synchronized with the driving signal of line frequency switches Q_1 and Q_3. When Clock1 is at "1," the output signal of the S&H, $P_{\text{pv\_sample}}$, tracks its input signal. Conversely, when Clock1 is at "0," $P_{\text{pv\_sample}}$ remains constant. Clock2 is generated by delaying the rising edge of Q_2 and Q_4 using a basic *RC* delay circuit. The D-type flip-flop updates the perturbation direction of the next P_{ref} at the rising edge of Clock2. Therefore, the perturbation period of the MPPT controller equals the line cycle T_L.

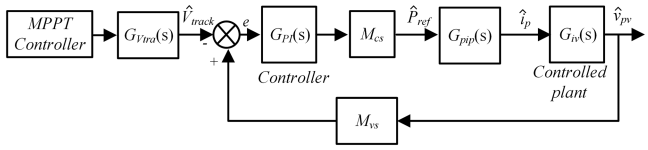

Fig. 9. Small-signal model of the voltage control loop.

Due to the presence of the double-line frequency fluctuations in the PV output power as shown in the top of Fig. 8, arbitrarily designed clocks may result in an inaccurate determination of $V_{\text{pw\_dir}}$. To cover this issue, the time duration between the falling edge of Clock1 and the rising edge of Clock2 is set to half a line cycle, thereby accurately filtering out the double-line frequency component.

All clocks in the MPPT circuit are derived from the driving signals of unfolding bridge MOSFETs, avoiding using precise timers. The accurate time duration between Clock1 and Clock2 can eliminate misjudgment issues without using extra signal conditioning circuits. In summary, by adopting the analog MPPT strategy, a simple and high-performance MPPT circuit can be obtained.

E. Design of Voltage Loop

Assuming the voltage control loop is disabled, and the value of P_{ref} is equal to the capacitor voltage V_{track}. As a result, the step size is directly determined by the state of the capacitor C_m, making it uncontrollable. The fixed-step MPPT strategy may become unstable due to an unsuitable perturbation step size [38]. Similarly, the analog scheme may experience instability under varying irradiation conditions due to the uncontrollable perturbation step size. Additionally, due to the periodic MPPT operation, there is a hysteresis between the perturbation command, P_{ref}, and the actual active output power. This hysteresis exacerbates power oscillations and may lead to instability near the MPP.

To solve these problems, a single voltage loop consisting of a PI controller is utilized to enhance the system's stability. The transfer function of the PI controller can be expressed as

$$G_{PI}(s) = k_P \frac{T_i s + 1}{T_i s} \tag{16}$$

where k_P is the proportional coefficient, T_i is the integral time constant, and the integral coefficient k_I equals k_P/T_i.

To simplify the analysis, all small-signal equations are established around the MPP, and the PV voltage fluctuations are neglected. The small-signal model of the voltage control loop is constructed from the voltage reference, V_{track}, to the PV voltage, as shown in Fig. 9, where M_{cs} represents the current sensing gain and M_{vs} represents the voltage sensing gain. The small-signal transfer function derivations for each unit are conducted as follows.

Similar to the operation of dc/dc converters, by using the average model of capacitor C_m over a switching cycle, the transfer function from V_{flag2}'s duty cycle to V_{track} can be expressed as

$$G_{\text{Vtra}}(s) = \frac{\hat{V}_{\text{track}}}{\hat{d}_{\text{flag2}}} = \frac{-V_{\text{dc}}}{R_{\text{char}} C_m s + 1} \tag{17}$$

where symbols with hats represent small-signal variations around the steady-state value.

Similar to the control-to-output transfer function of the DCM inverter [41], under PCC, the output current and output power of the BCM inverter are directly determined by the control command. Furthermore, as previously stated, a hysteresis exists between P_{ref} and the actual active output power due to the periodic updating operation. Therefore, the transfer function from $\hat{P}_{\text{ref}}$ to $\hat{i}_p$ can be modeled as a first-order inertial element, characterized by a time constant T_L, which equals the MPPT cycle

$$G_{\text{pip}}(s) = \frac{\hat{i}_p}{\hat{P}_{\text{ref}}} = \frac{1}{T_L s + 1} \frac{2}{V_{\text{mpp}}} \tag{18}$$

where V_{mpp} is the MPP voltage. In small-signal analysis, the PV module could be seen as a resistor R_{mpp} at steady-state [39]

$$\hat{v}_{\text{pv}} = -R_{\text{mpp}} \hat{i}_{\text{pv}}. \tag{19}$$

The microinverter, positioned downstream of the decoupling capacitors, could be considered a current source [13]. Therefore, the small-signal transfer function from $\hat{i}_p$to $\hat{v}_{\text{pv}}$ is derived using the average model of decoupling capacitors over a switching cycle

$$G_{iv}(s) = \frac{\hat{v}_{\text{pv}}}{\hat{i}_p} = \frac{-R_{\text{mpp}}}{R_{\text{mpp}} C_{\text{in}} s + 1}. \tag{20}$$

When employing the PI controller, the open-loop transfer function can be derived as

$$\begin{aligned} G_{\text{PI\_on}}(s) &= G_{\text{Vtra}}(s) G_{\text{PI}}(s) G_{\text{pip}}(s) G_{\text{iv}}(s) M_{\text{vs}} M_{\text{cs}} \\ &= K_{\text{OL}} \frac{T_i s + 1}{s} \frac{1}{R_{\text{char}} C_m s + 1} \frac{1}{T_L s + 1} \frac{1}{R_{\text{mpp}} C_{\text{in}} s + 1} \end{aligned} \tag{21}$$

where K_{OL} represents the open-loop gain. Fig. 10 shows the open-loop bode diagram of the compensated system, $G_{\text{PI\_ON}}(s)$, where $k_P = 0.005$, $k_I = 0.01$, $V_{\text{dc}} = 10$ V, $R_{\text{char}} = 100$ kΩ, $C_m = 10$ μF, $V_{\text{mpp}} = 36$ V, $R_{\text{mpp}} = 10.368$ Ω, $T_L = 0.02$, $C_{\text{in}} = 8800$ μF, $Mvs = 0.25$, and $Mcs = 10$. It is possible to increase the phase margin, γ_2, to a stable threshold value of 30° by adjusting the value of K_{OL} while maintaining an appropriate magnitude margin according to (21). This ensures the stability of the closed-loop system.

As a comparison, the system open-loop transfer function without the PI controller can be represented as (22). The bode plot of $G_{\text{PI\_OFF}}(s)$ in Fig. 10 shows a phase margin γ_1 significantly smaller than 30°, leading to MPPT instability

$$\begin{aligned} G_{\text{PI\_off}}(s) = &\frac{2 R_{\text{mpp}} V_{\text{dc}} M_{\text{cs}}}{V_{\text{mpp}}} \frac{1}{R_{\text{char}} C_m s + 1} \frac{1}{T_L s + 1} \\ &\times \frac{1}{R_{\text{mpp}} C_{\text{in}} s + 1}. \end{aligned} \tag{22}$$

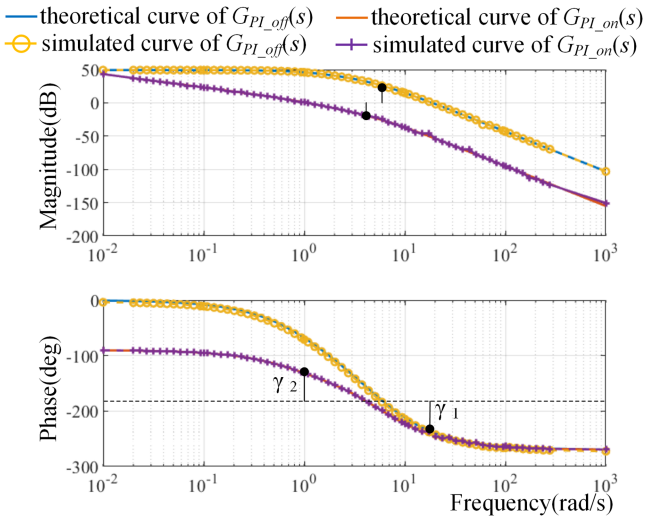

Fig. 10. Bode diagram of the open-loop transfer function.

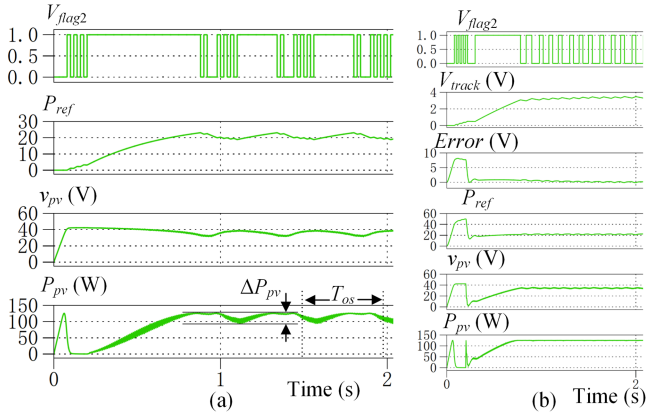

Fig. 11. (a) Unstable MPPT without the compensator. (b) Stable MPPT with the compensator.

Fig. 11(b) shows the stable MPPT control waveforms with a PI controller (where $k_P = 0.005$ and $k_I = 0.01$), ensuring a phase margin greater than 30° according to (21). In contrast, Fig. 11(a) shows unstable MPPT control without the PI controller, where P_{ref} is equal to the capacitor voltage V_{track}. An inadequate phase margin results in a low-frequency power oscillation of 30 W (ΔP_{pv}) with a frequency of 2.2 Hz ($1/T_{\text{os}}$).

III. Design Considerations

This section addresses the tradeoff between enhancing power conversion efficiency and managing circuit complexity in the analog scheme. Additionally, considerations for circuit parameters to eliminate the effects of signal transmission delay and quasi-resonant (QR) time on the THD of the grid-connected current are also presented.

For flyback microinverters, it is important to determine the turns ratio and magnetizing inductance first, and then optimize the remaining circuit parameters. The turns ratio N can be determined by [18]

$$N = V_g / (\eta v_{\text{pv}}) \tag{23}$$

where η is the estimated conversion efficiency and is set as 0.9, therefore, N is set as 6. The magnetizing inductance can be designed as [18]

$$L_m = \frac{v_{\text{pv}} d_{\max}}{i_{p\_\text{peak},\max} f_{s\_\min}} \tag{24}$$

where $d_{\max}$ is the maximum duty cycle and is set as 0.5 according to the design of the traditional flyback converter. $f_{s\_\min}$ is the minimum switching frequency and is designed as 200 kHz. Accordingly, the initial value of magnetizing inductance is 3.78 μH.

A. Efficiency Improvement

It is well known that the active clamping technology [8] can recover the leakage energy, but it needs extra MOSFETs and drive circuits. The QR technique is widely studied to reduce the turn-ON loss of the main switch [15], and a digital controller [15] or an elaborately designed analog circuit for valley detection [37] is usually employed to accurately determine the QR time. The fixed QR technique [18] can be realized with simple analog components, where the QR time is designed as a fixed value $t_{\text{QR\_fixed}}$. Therefore, this article applies the fixed QR technique to improve the power conversion efficiency, while avoiding excessive circuit costs.

B. Analysis of the Grid-Connected Current's THD

The presence of the hysteresis comparator and the RS flip-flop with the input threshold voltage will cause an undesired transmission delay t_{d_OFF} in the turn-OFF signal of the main switch. Both t_{d_OFF} and $t_{\text{QR\_fixed}}$ significantly affect the THD of the grid-connected current.

To simplify the analysis, it is assumed that there are no power losses. Considering $t_{\text{QR\_fixed}}$ [18] and t_{d_OFF}, the average value of the secondary current becomes

$$i_{s\_\text{avg}}(\theta_g) = \sqrt{2} I_g \sin(\theta_g) \cdot A(\theta_g) + B(\theta_g) \tag{25}$$

where $A(\theta_g)$ and $B(\theta_g)$ are distortion coefficients

$$A(\theta_g) = \frac{1 + \frac{N v_{\text{pv}}}{\sqrt{2} V_g \sin(\theta_g)}}{1 + \frac{N v_{\text{pv}}}{\sqrt{2} V_g \sin(\theta_g)} + \frac{t_{\text{QR\_fixed}}}{t_{\text{on}}(\theta_g) + t_{d\_\text{off}}}} \tag{26}$$

$$B(\theta_g) = \frac{1}{2} \frac{v_{\text{pv}}}{N L_m} t_{d\_\text{off}} \frac{N v_{\text{pv}}}{\sqrt{2} V_g \sin(\theta_g) + N v_{\text{pv}}} A(\theta_g). \tag{27}$$

The numerical curves of $A(\theta_g)$ and $B(\theta_g)$ over half a line cycle can be obtained according to (26) and (27), as shown in Fig. 12. $A(\theta_g)$ keeps almost constant (0.869–0.951) over a wide range of θ_g (0.14 rad–3 rad). Moreover, the value of $B(\theta_g)$ is significantly affected by the high switching frequency in the zero-crossing region. To suppress the current distortion, the minimum switching frequency can be adjusted from 200 to 110 kHz. Therefore, the magnetizing inductance is adjusted from 3.78 to 6.86 μH according to (24), resulting in a 50% decrease in $B(\theta_g)$ and a narrower variation range (0.915–0.965) of $A(\theta_g)$.

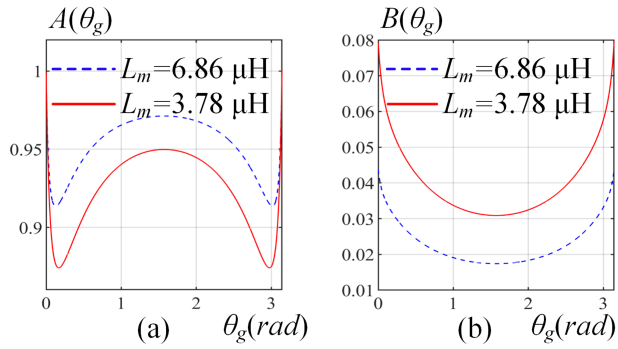

Fig. 12. Calculated values of (a) A(θ_g) and (b) B(θ_g) over half a line frequency.

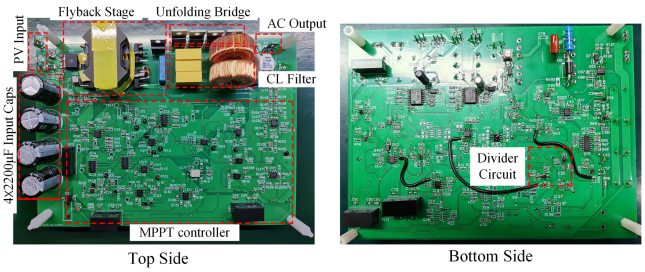

Fig. 13. BCM flyback microinverter prototype.

TABLE II
CIRCUIT PARAMETERS

Parameter	Symbol	Value
Rated power	P_R	125 W
PV voltage	v_{pv}	30–50 V
Voltage@MPP	V_{mpp}	36 V
Decoupling capacitance	C_{in}	4 × 2200 μF
Transformer turns-ratio	N	6
Magnetizing inductance	L_m	6.86 μH
Fixed QR time	$t_{\text{QR\_fixed}}$	230 ns
Dead time of unfolding bridge	t_{dead}	160 μs
Transmission delay	t_{d_OFF}	100 ns
RMS value of the i_g	I_g	0.568A/ac ,50 Hz
RMS value of grid voltage	V_g	220V/ac,50 Hz

TABLE III
KEY PERFORMANCE INDICATORS AT RATED POWER

Parameter	Value
Static MPPT efficiency	99.5%
Peak conversion efficiency	94.1%
Power factor	0.999
THD	2.75%

IV. EXPERIMENTAL RESULTS

A 125 W BCM flyback microinverter prototype at 220 V/50 Hz utility condition is implemented to validate the proposed analog control strategy. The microinverter prototype is shown in Fig. 13, and the circuit parameters are shown in Table II. Key performance indicators at rated power are presented in Table III.

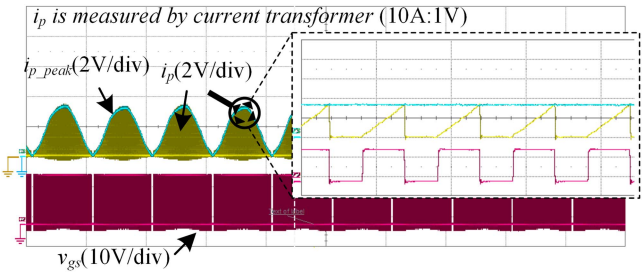

Fig. 14. Experimental waveforms of the primary current.

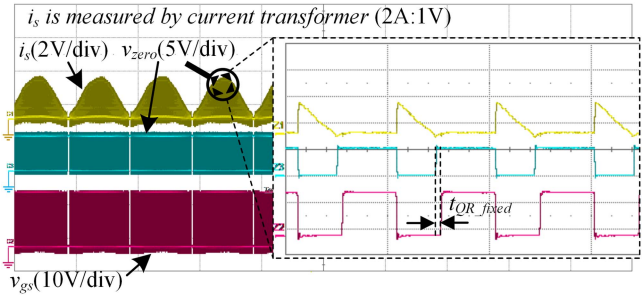

Fig. 15. Experimental waveforms of the secondary current.

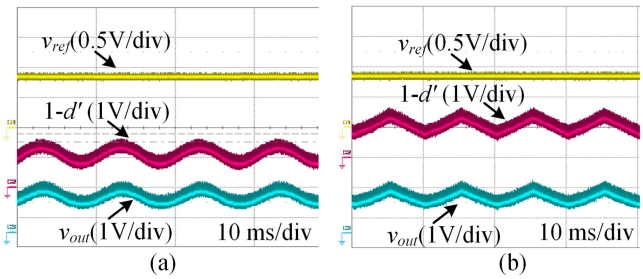

Fig. 16. Typical waveforms of the dedicated divider. (a) Sinusoidal modulating signal is applied to d'. (b) Triangular modulating signal is applied to d'.

Fig. 14 shows the experimental waveforms of the primary current, which is measured by a CT with the ratio of 10 A:1 V. It is clear that the envelope of the primary current overlaps with the proposed current reference (3). Fig. 15 shows the experimental waveforms of the secondary current i_s, which is measured by a CT with the ratio of 2 A:1 V. The QR operation of the main switch can be achieved by applying a fixed time delay $t_{\mathrm{QR\_fixed}}$ following the raising edge of v_{zero}.

The analog divider's dynamic response is shown in Fig. 16, where a sinusoidal modulating signal ($v_{\mathrm{modu}} = 0.5\sin(\omega t)+1$) at 50 Hz is compared with a triangular signal with a peak value of 3 V to produce $d' = \frac{2-0.5\sin(\omega t)}{3}$. The circuit is powered by a +5 V supply, and the reference input signal is constant ($v_{\mathrm{ref}} = 0.833$ V). DC transfer curve measurements are performed, as illustrated in Fig. 17, with less than 2% deviation in output, indicated by the solid green line. The output error remained below 1% within the commonly used range of d' (0.4–0.6). This demonstrates the high accuracy of the proposed analog divider.

Table IV compares divider circuits implemented with discrete ICs, including resistors and capacitors. Unit prices are from publicly available e-commerce websites. The proposed divider

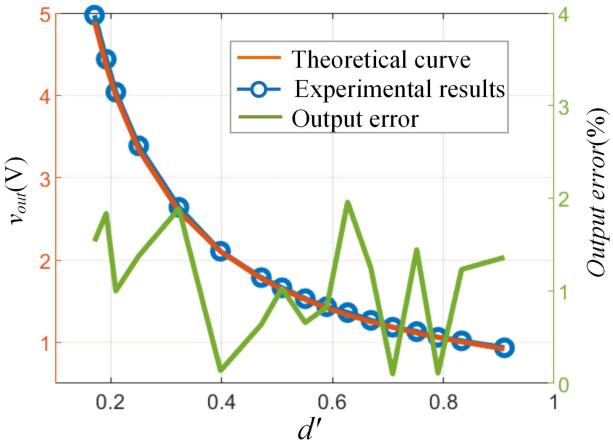

Fig. 17. Theoretical and experimental DC transfer curves.

TABLE IV
COMPARISON OF DIVIDER CIRCUIT

	[33]	[34]	[35]	This work
Input signal	Voltage	Voltage	Voltage	Voltage
Output signal	Voltage	Voltage	Voltage	Voltage
Range of numerator	±1 V	N/A	±0.5 V	0−5 V
Range of denominator	±1 V	0−10 V	0−1 V	0−1
Max. error	<3.5%	<0.5%@ Denominator's range: 0.3 V−3 V	<5%	**<2%**
Components	3×OTA; 1×Cap	2×Monostable; 1×VCO; 2×OA; 2×Analog Switch; 2×Cap; 1×Res	15×MOS Array; 1×Cap	**2×Analog Switch; 1×OA; 1×Cap; 2×Res**
Cost ($)	3.74	11.77	3.91	**0.45**

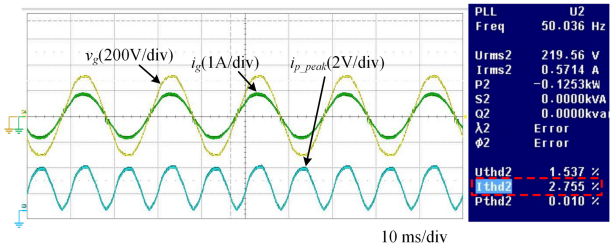

Fig. 18. Grid-connected current as L_m is set to 6.86 μH.

uses the fewest components and offers good accuracy. Other dividers require additional signal conversion circuits to perform the division operation in (3), demonstrating the simplicity and cost-effectiveness of the proposed divider.

Fig. 18 shows the experimental waveforms of grid-connected current with the proposed divider. To limit the switching frequency, a dead zone is utilized in the zero-crossing region, resulting in a slight distortion of the grid-connected current i_g. The measured THD of i_g is 2.75% and the PF value is 0.999. The THD of i_g at different power levels is shown in Table V, which meets IEC61727 and IEEE1547 standards quite well.

Fig. 19 illustrates the experimental waveforms of the sampling signals and clocks in the MPPT circuit. The pulsewidth of Clock2 is set to 400 μs, thereby ensuring that the time duration

TABLE V
THD OF GRID-CONNECTED CURRENT UNDER DIFFERENT OUTPUT POWER

P_{pv}	45 W	65 W	85 W	105 W	125 W
THD	4.5%	3.2%	2.9%	2.7%	2.7%

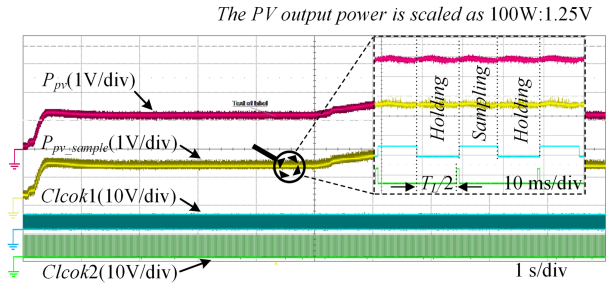

Fig. 19. Sampling signals and clocks in the MPPT circuit.

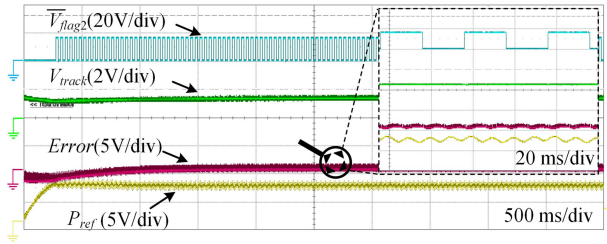

Fig. 20. Experimental waveforms of the MPPT controller under constant irradiation.

TABLE VI
EXPERIMENTAL STATIC MPPT EFFICIENCIES

P_{pv}/P_{MPP}	η_{static}	P_{pv}/P_{MPP}	η_{static}
10%	99.3%	60%	99.3%
20%	99.5%	70%	99.6%
30%	99.2%	80%	99.7%
40%	99.2%	90%	99.8%
50%	99.4%	100%	99.5%

between the rising edge of Clock2 and the falling edge of Clock1 equals half a line cycle.

Experimental waveforms of the PI controller under constant irradiation are depicted in Fig. 20. In this circuit setup, V_{Flag2} is responsible for regulating the voltage reference V_{track}. The PI controller has the characteristic of variable step size, which can effectively reduce the power oscillation around the MPP.

Using the analog MPPT strategy, the static MPPT efficiency at rated PV power can reach over 99.5%, which is obtained from the software panel of array simulator Sorensen DCS80-15E, as shown in Fig. 21. Table VI summarizes the experimental static MPPT efficiencies of the proposed MPPT controller at different percentages of MPP power.

Fig. 22 compares the experimental dynamic efficiencies of the analog MPPT controller and the digital P&O MPPT controller under the EN50530 test standard [40]. The digital fixed-step P&O MPPT controller is implemented using the TI TMS320F28335, with the step size set to $\Delta P_{ref} = 2.5$ W (0.02 of

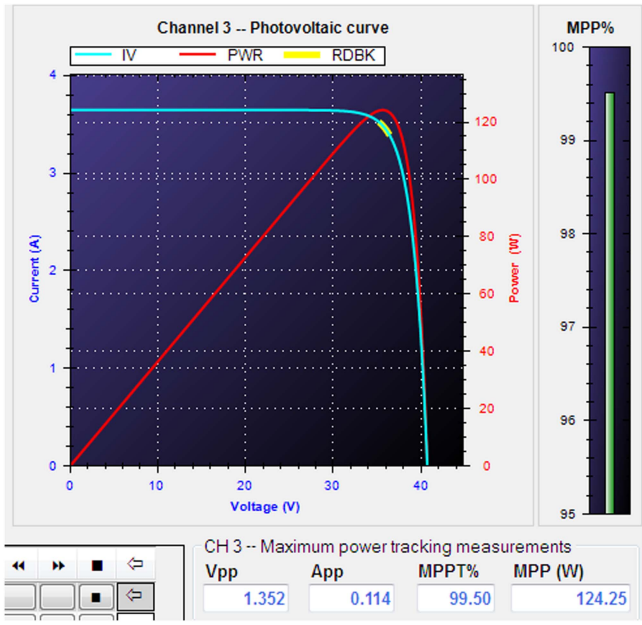

Fig. 21. MPPT efficiency of BCM flyback microinverter.

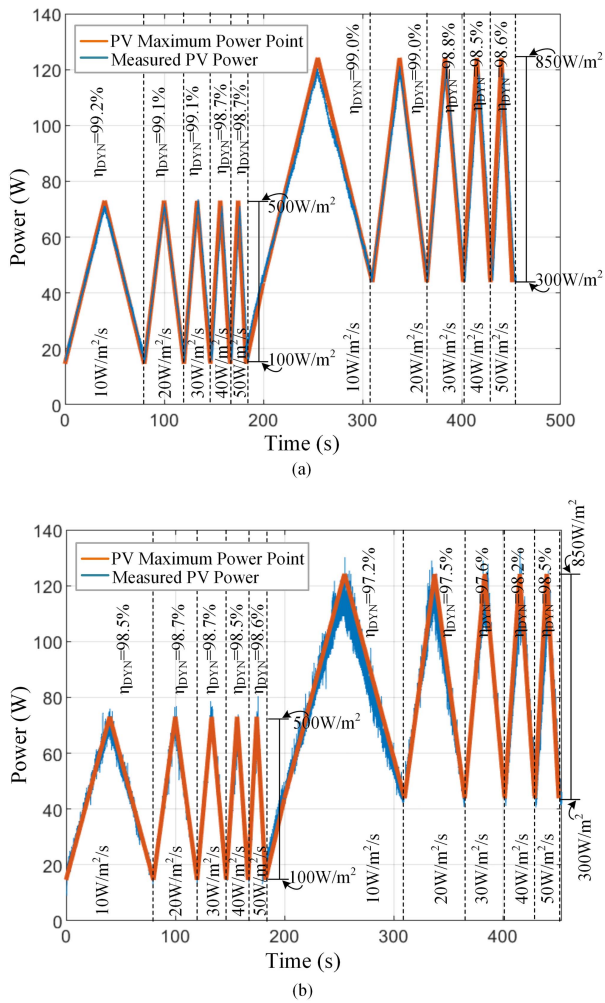

Fig. 22. Comparisons of experimental dynamic efficiencies under the EN50530 standard between (a) analog MPPT controller and (b) digital P&O MPPT controller.

TABLE VII
COMPARISON OF BCM FLYBACK MICROINVERTER

Parameter	[14]	[20]	[15]	[18]	This work
Modulation	On-time	Peak-current	Peak-current	Peak-current	Peak-current
Rated power	205 W	250 W	200 W	200 W	125 W
Topology	Single-phase	Single-phase	Two-phase Interleaving	Two-phase Interleaving	Single-phase
Transformer's core	ETD54	EE55	2×RM14	2×RM14	RM14
Core's power density	5.77 W/cm^3	5.72 W/cm^3	8 W/cm^3	8 W/cm^3	10 W/cm^3
MPPT algorithm	N/A	N/A	Perturb & observe	Incremental conductance	Analog MPPT strategy
MPPT efficiency	N/A	N/A	N/A	N/A	99.5%
Peak efficiency	>93%	>93%	>94%	>94%	94.1%
CEC efficiency	91.5%	N/A	92.68%	N/A	93.1%
THD	3.77%	N/A	4.2%	2.459%	2.75%
Compensator	Open loop	Type III compensator	Open loop	Open loop	PI controller
Hardware implementation	DSPIC30f4011	TMSF28335+DAC +Comparator	EP3C10E+DAC+ Comparator	EP3C10E144+DAC+ Comparator	Discrete analog ICs

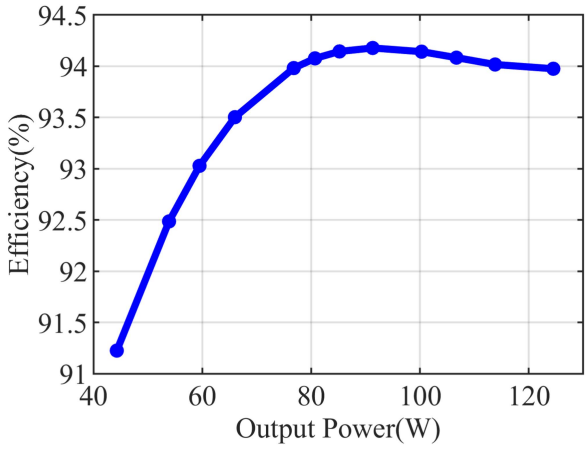

Fig. 23. Measured efficiency versus output power.

rated PV power) and an MPPT update rate of 25 Hz. Due to the limited storage capacity of the oscilloscope (Teledyne LeCroy 3054z), the efficiency was only evaluated under fast-changing irradiation conditions. The PV MPP voltage ranges from 32 V at 100 W/m^2 to 36 V at 850 W/m^2, with a constant temperature of 25 °C. Ten subtests were performed with varying irradiation change rates (10–50 W/m^2/s) and ranges (100–500 W/m^2 and 300–850 W/m^2). The average dynamic efficiency (η_{DYN}) of the analog MPPT controller is 98.8%, compared to 97.5% for the digital MPPT controller. The fixed-step size algorithm [21], [39] and inappropriate perturbation period [21] may fail to provide optimal dynamic tracking performance across a wide range of irradiation change rates, while commercial microinverters typically achieve efficiencies above 99% using optimized variable step size algorithms. However, algorithm optimization is not the focus of this article.

Fig. 23 shows the experimental data of conversion efficiency versus output power, which is measured by Yokogawa WT500. The peak efficiency achieved in this article is 94.1%, and the weighted CEC efficiency is 93.1%.

V. DISCUSSION

Table VII compares various control schemes for the BCM flyback microinverter, showing that the proposed method achieves comparable or superior performance in THD and MPPT efficiency, while maintaining low costs. These advantages lead to broad application prospects in cost-sensitive PV applications, including efficiency optimization, cost reduction, and power density improvement.

Regarding power conversion efficiency, Rezaei et al. [16] report 94.6% weighted CEC efficiency with a DCM/BCM interleaved flyback microinverter. Although the prototype only achieved 93.1% efficiency without advanced optimization techniques, its simplified circuit design allows easy integration with methods such as active snubbers, hybrid conduction modes, and interleaving control. For example, the analog interleaving control [25] can be integrated into the proposed control strategy through minor modifications to the modulation technique of the primary switch.

Cost remains a significant barrier to microinverter adoption. ICs and their peripheral circuits account for approximately 20% of the electronic material costs in microinverters [3], with the control circuit being a major contributor. Implementing the PCC typically requires microcontrollers, DACs, and comparators [15], [18], [20], which increases the overall cost compared to the proposed method that relies on discrete ICs. This demonstrates the cost advantage of dedicated analog control strategies in specific applications. The simplified design also leads to savings in areas such as PCB design, enclosure, and installation. Therefore, analog control strategies offer substantial advantages for cost-sensitive PV applications.

In terms of power density, CCM has higher core utilization than BCM and DCM. The hysteresis control method is typically employed in CCM to achieve grid-connected control, and its operating principle is similar to that of the PCC, with the current reference calculation in CCM identical to BCM. Therefore, the proposed analog control strategy can be utilized to simplify the hardware implementation of CCM.

VI. CONCLUSION

A dedicated analog control strategy is a promising way to improve the competitiveness of the BCM flyback microinverter in cost-sensitive applications. Under the analog scheme, traditional grid-connected control and MPPT methods face the problems of complex circuit structures and high circuit costs.

This article explores a low-cost analog control strategy for BCM flyback microinverters, aiming to achieve high-performance grid-connected control and MPPT using the simplest circuit structure and a minimal number of components. The key innovations of this article can be summarized as follows.

1) A dedicated analog divider circuit is proposed to perform the customized division operation, enabling the achievement of well-sinusoidal grid-connected current and high PF using only three low-cost analog components.
2) An analog MPPT strategy is proposed, featuring optimal perturbation logic and control timing to simplify hardware implementation and eliminate misjudgment issues. This strategy enables high static and dynamic efficiencies while utilizing a straightforward circuit design and a minimal number of basic components.
3) This control strategy features simplified circuit design, enabling easy integration with other efficiency optimization methods and compatibility with flyback-based applications.

The experimental results on a 125 W prototype demonstrate that the proposed analog control strategy can achieve high MPPT efficiency, high power quality, and high conversion efficiency through a simple circuit structure. It also lays the foundation for future article on dedicated control chips.

Acknowledgment

The author would like to thank ZJU-PLEXIM Joint Simulation Laboratory for the support of the powerful simulation tool PLECS.

References

[1] H. Hu, S. Harb, N. Kutkut, I. Batarseh, and Z. J. Shen, "A review of power decoupling techniques for microinverters with three different decoupling capacitor locations in PV systems," *IEEE Trans. Power Electron.*, vol. 28, no. 6, pp. 2711–2726, Jun. 2013, doi: 10.1109/TPEL.2012.2221482.

[2] "Solar microinverter market size, share & trends analysis report, 2024–2030," Grand View Research, 2024.

[3] M. Chen et al., "An analog control strategy with multiplier-less power calculation circuit for flyback microinverter," *IEEE Trans. Power Electron.*, vol. 36, no. 8, pp. 8617–8621, Aug. 2021, doi: 10.1109/TPEL.2021.3056382.

[4] InfoLink Consulting, "PV supply chain price trend for 2024," Mar. 2024. [Online]. Available: https://www.infolink-group.com/energy-article/solar-topic-2024-solar-supply-chain-price-trend

[5] "Best research-cell efficiencies," National Renewable Energy Laboratory, 2024. [Online]. Available: https://www.nrel.gov/pv/cellefficiency.html/

[6] "Establishing a network code on requirements for grid connection of generators," The European Commission, Official Journal of the European Union, no. 2016/631, 2016. [Online]. Available: https://eur-lex.europa.eu/legal-content/EN/TXT/PDF/?uri=CELEX:32016R0631

[7] H. Wirth, "Recent facts about photovoltaics in Germany - Fraunhofer ISE," Fraunhofer Inst. Solar Energy Syst. ISE, 2019. [Online]. Available: https://www.ise.fraunhofer.de/en/publications/studies/recent-facts-about-pv-in-germany.html

[8] Q. Mo, M. Chen, Z. Zhang, Y. Zhang, and Z. Qian, "Digitally controlled active clamp interleaved flyback converters for improving efficiency in photovoltaic grid-connected micro-inverter," in *Proc. 27th Annu. IEEE Appl. Power Electron. Conf. Expo.*, 2012, pp. 555–562, doi: 10.1109/APEC.2012.6165874.

[9] E. Dzhunusbekov and S. Orazbayev, "A new passive lossless snubber," *IEEE Trans. Power Electron.*, vol. 36, no. 8, pp. 9263–9272, Aug. 2021, doi: 10.1109/TPEL.2021.3056189.

[10] Y. Wang, Y. Zhang, Q. Mo, M. Chen, and Z. Qian, "An improved control strategy based on multiplier for CRM flyback PFC to reduce line current peak distortion," in *Proc. IEEE Energy Convers. Congr. Expo.*, 2010, pp. 901–905, doi: 10.1109/ECCE.2010.5617898.

[11] D. G. Lamar, J. S. ZÚÑiga, A. R. Alonso, M. R. GonzÁlez, and M. M. H. Álvarez, "A very simple control strategy for power factor correctors driving high-brightness LEDs," *IEEE Trans. Power Electron.*, vol. 24, no. 8, pp. 2032–2042, Aug. 2009, doi: 10.1109/TPEL.2009.2020900.

[12] J. Zhang, H. Zeng, and T. Jiang, "A primary-side control scheme for high-power-factor LED driver with TRIAC dimming capability," *IEEE Trans. Power Electron.*, vol. 27, no. 11, pp. 4619–4629, Nov. 2012, doi: 10.1109/TPEL.2012.2187341.

[13] G. C. Christidis, A. C. Nanakos, and E. C. Tatakis, "Hybrid discontinuous/boundary conduction mode of flyback microinverter for AC–PV modules," *IEEE Trans. Power Electron.*, vol. 31, no. 6, pp. 4195–4205, Jun. 2016, doi: 10.1109/TPEL.2015.2470094.

[14] A. C. Nanakos, G. C. Christidis, and E. C. Tatakis, "Weighted efficiency optimization of flyback microinverter under improved boundary conduction mode (i-BCM)," *IEEE Trans. Power Electron.*, vol. 30, no. 10, pp. 5548–5564, Oct. 2015, doi: 10.1109/TPEL.2014.2372005.

[15] Z. Zhang, M. Chen, W. Chen, C. Jiang, and Z. Qian, "Analysis and implementation of phase synchronization control strategies for BCM interleaved flyback microinverters," *IEEE Trans. Power Electron.*, vol. 29, no. 11, pp. 5921–5932, Nov. 2014, doi: 10.1109/TPEL.2014.2300483.

[16] M. A. Rezaei, K.-J. Lee, and A. Q. Huang, "A high-efficiency flyback micro-inverter with a new adaptive snubber for photovoltaic applications," *IEEE Trans. Power Electron.*, vol. 31, no. 1, pp. 318–327, Jan. 2016, doi: 10.1109/TPEL.2015.2407405.

[17] Y.-H. Kim, Y.-H. Ji, J.-G. Kim, Y.-C. Jung, and C.-Y. Won, "A new control strategy for improving weighted efficiency in photovoltaic AC module-type interleaved flyback inverters," *IEEE Trans. Power Electron.*, vol. 28, no. 6, pp. 2688–2699, Jun. 2013, doi: 10.1109/TPEL.2012.2226753.

[18] M. Gao, M. Chen, C. Zhang, and Z. Qian, "Analysis and implementation of an improved flyback inverter for photovoltaic AC module applications," *IEEE Trans. Power Electron.*, vol. 29, no. 7, pp. 3428–3444, Jul. 2014, doi: 10.1109/TPEL.2013.2279266.

[19] Z. Zhang, X.-F. He, and Y.-F. Liu, "An optimal control method for photovoltaic grid-tied-interleaved flyback microinverters to achieve high efficiency in wide load range," *IEEE Trans. Power Electron.*, vol. 28, no. 11, pp. 5074–5087, Nov. 2013, doi: 10.1109/TPEL.2013.2245919.

[20] N. Sukesh, M. Pahlevaninezhad, and P. K. Jain, "Analysis and implementation of a single-stage flyback PV microinverter with soft switching," *IEEE Trans. Ind. Electron.*, vol. 61, no. 4, pp. 1819–1833, Apr. 2014, doi: 10.1109/TIE.2013.2263778.

[21] Z. Zhang, W. Chen, and M. Chen, "Optimization of the maximum power point tracking method for peak-current controlled flyback microinverter," in *Proc. IEEE Energy Convers. Congr. Expo.*, 2014, pp. 800–805, doi: 10.1109/ECCE.2014.6953478.

[22] R. Enne, M. Nikolić, and H. Zimmermann, "Dynamic integrated MPP tracker in 0.35 μm CMOS," *IEEE Trans. Power Electron.*, vol. 28, no. 6, pp. 2886–2894, Jun. 2013, doi: 10.1109/TPEL.2012.2213615.

[23] C. Wang, M. Chen, X. Zhang, and M. Gao, "An analog MPPT controller without multiplier for PV applications based on simplified P&O method," in *Proc. IEEE Energy Convers. Congr. Expo.*, 2017, pp. 2296–2300, doi: 10.1109/ECCE.2017.8096446.

[24] S. J. Yaqoob et al., "Flyback photovoltaic micro-inverter with a low cost and simple digital-analog control scheme," *Energies*, vol. 14, no. 14, 2021, Art. no. 4239.

[25] E. M. Najm, A. Q. Huang, and W. Yu, "A novel low cost PV micro-inverters based on analog control and interleaving method," in *Proc. IEEE Appl. Power Electron. Conf. Expo.*, 2015, pp. 221–228, doi: 10.1109/APEC.2015.7104355.

[26] T. Yan, J. Xu, F. Zhang, J. Sha, and Z. Dong, "Variable-on-time-controlled critical-conduction-mode flyback PFC converter," *IEEE Trans. Ind. Electron.*, vol. 61, no. 11, pp. 6091–6099, Nov. 2014, doi: 10.1109/TIE.2014.2311401.

[27] Z. Lai and K. M. Smedley, "A family of continuous-conduction-mode power-factor-correction controllers based on the general pulse width modulator," *IEEE Trans. Power Electron.*, vol. 13, no. 3, pp. 501–510, May 1998.

[28] R. Enne, M. Nikolic, and H. Zimmermann, "A maximum power-point tracker without digital signal processing in 0.35 μm CMOS for automotive applications," in *Proc. IEEE Int. Solid-State Circuits Conf.*, 2012, pp. 102–104, doi: 10.1109/ISSCC.2012.6176894.

[29] Y. Sugimoto, "The solar cells and the battery charger system using the fast and precise analog maximum power point tracking circuits," in *Proc. IEEE Comput. Soc. Annu. Symp. VLSI*, 2015, pp. 597–602, doi: 10.1109/ISVLSI.2015.36.

[30] F. Liu, Y. Han, Y. Gao, and J. Sun, "An analog MPPT controller IC together with its application circuit," *IEICE Electron. Exp.*, vol. 11, no. 20, pp. 1–6, 2014.

[31] H. S.-H. Chung, K. K. Tse, S. Y. R. Hui, C. M. Mok, and M. T. Ho, "A novel maximum power point tracking technique for solar panels using a SEPIC or Cuk converter," *IEEE Trans. Power Electron.*, vol. 18, no. 3, pp. 717–724, May 2003, doi: 10.1109/TPEL.2003.810841.
[32] P. Mattavelli, S. Saggini, E. Orietti, and G. Spiazzi, "A simple mixed-signal MPPT circuit for photovoltaic applications," in *Proc. 25th Annu. IEEE Appl. Power Electron. Conf. Expo.*, 2010, pp. 953–960, doi: 10.1109/APEC.2010.5433389.
[33] E. Sanchez-Sinencio, J. Ramirez-Angulo, B. Linares-Barranco, and A. Rodriguez-Vazquez, "Operational transconductance amplifier-based nonlinear function synthesis," *IEEE J. Solid-State Circuits*, vol. 24, no. 6, pp. 1576–1586, Dec. 1989.
[34] T. L. Laoppoulos and C. A. Karybakas, "A simple analog division scheme," *IEEE Trans. Instrum. Meas.*, vol. 40, no. 4, pp. 779–782, Aug. 1991.
[35] S.-I. Liu and C.-C. Chang, "CMOS analog divider and four-quadrant multiplier using pool circuits," *IEEE J. Solid-State Circuits*, vol. 30, no. 9, pp. 1025–1029, Sep. 1995.
[36] C. Zhao, J. Zhang, and X. Wu, "An improved variable on-time control strategy for a CRM flyback PFC converter," *IEEE Trans. Power Electron.*, vol. 32, no. 2, pp. 915–919, Feb. 2017, doi: 10.1109/TPEL.2016.2594201.
[37] W.-C. Wu, T.-J. Liang, K.-H. Chen, and C.-Y. Li, "Quasi-resonant flyback converter with new valley voltage detection mechanism," in *Proc. IEEE Appl. Power Electron. Conf. Expo.*, 2018, pp. 767–770, doi: 10.1109/APEC.2018.8341098.
[38] W. Libo, Z. Zhengming, L. Jianzheng, L. Shu, and Y. Liqiang, "Modified MPPT strategy applied in single-stage grid-connected photovoltaic system," in *Proc. Int. Conf. Elect. Mach. Syst.*, 2005, pp. 1027–1030, doi: 10.1109/ICEMS.2005.202702.
[39] N. Femia, G. Petrone, G. Spagnuolo, and M. Vitelli, "Optimization of perturb and observe maximum power point tracking method," *IEEE Trans. Power Electron.*, vol. 20, no. 4, pp. 963–973, Jul. 2005, doi: 10.1109/TPEL.2005.850975.
[40] *Overall Efficiency of Grid Connected Photovoltaic Inverters*, Standard EN505030, Apr. 2010.
[41] S.-H. Lee, W.-J. Cha, J.-M. Kwon, and B.-H. Kwon, "Control strategy of flyback microinverter with hybrid mode for PV AC modules," *IEEE Trans. Ind. Electron.*, vol. 63, no. 2, pp. 995–1002, Feb. 2016, doi: 10.1109/TIE.2015.2481365.
[42] M. S. Irfan, J.-H. Shin, and J.-H. Park, "New control method for power decoupling of electrolytic capacitor-less photovoltaic micro-inverter with primary side regulation," *J. Elect. Eng. Technol.*, vol. 13, no. 2, pp. 677–687, 2018, doi: 10.5370/JEET.2018.13.2.677.
[43] T. V. Thang, N. M. Thao, J.-H. Jang, and J.-H. Park, "Analysis and design of grid-connected photovoltaic systems with Multiple-integrated converters and a pseudo-DC-link inverter," *IEEE Trans. Ind. Electron.*, vol. 61, no. 7, pp. 3377–3386, Jul. 2014, doi: 10.1109/TIE.2013.2281153.

Celiang Deng received the B.S. degree in automation and the M.S. degree in control engineering from the Chongqing University, Chongqing, China, in 2019 and 2022, respectively. He is currently working toward the Ph.D. degree in electrical engineering with the College of Electrical Engineering, Zhejiang University, Hangzhou, China.

His research interests include the design, control, and optimization of high-efficiency grid-connected inverters and bidirectional converters in renewable energy systems.

Min Chen (Member, IEEE) received the B.S. degree in applied electronics and the Ph.D. degree in electrical engineering from the Zhejiang University, Hangzhou, China, in 2000 and 2006, respectively.

From 2007 to 2009, he was a Postdoctoral Researcher with the Department of Electrical Engineering, Zhejiang University. From 2010 to 2014, he was a Lecturer, and in 2014 was promoted as an Associate Professor. Since 2020, he has been a Full Professor with the Zhejiang University. From 2014 to 2015, he was a Visiting Researcher with the Department of Energy Technology, Aalborg University, Aalborg, Denmark. He has authored or coauthored more than 80 SCI/EI-indexed papers and was issued for almost 30 patents of inventions. He is currently the Director of ZJU Joint Research Center for New Energy and Power Electronics Based Power System and the Deputy Director of the National Engineering Research Center for Applied Power Electronics. His research interests include application of power electronics in power system, inverter and its control, renewable energy generation and grid connection, and bidirectional energy conversion technology for electric vehicle energy storage and charging.

Fan Zhang received the B.S. degree in electrical engineering from the Harbin Institute of Technology, Harbin, China, in 2022. He is currently working toward the Ph.D. degree in electrical engineering with the College of Electrical Engineering, Zhejiang University, Hangzhou, China.

His research interests include high-efficiency power conversion and cooperative stability control in renewable energy systems.

Ruirui Zheng received the B.S. degree in electrical Engineering, and the M.S. degree in power electronics from the Zhejiang University, Hangzhou, China, in 2020 and 2023, respectively.

He is currently employed with the MPS Inc., Hangzhou, China. During his master's studies, his research interests include analog control methods for flyback micro photovoltaic inverters.

Feng Jiang was born in Anhui Province, China. He received the M.S. degree in electrical engineering from the Zhejiang University, Hangzhou, China, in 2019.

He is currently an Assistant Researcher with the College of Electrical Engineering, Zhejiang University. His research interests include microgrid controller, application of power electronics in power system, and renewable energy.